

Entropy Landscaping of High-Entropy Carbides

Mohammad Delower Hossain,* Trent Borman, Corey Oses, Marco Esters, Cormac Toher, Lun Feng, Abinash Kumar, William G. Fahrenholtz, Stefano Curtarolo, Donald Brenner, James M. LeBeau, and Jon-Paul Maria

The entropy landscape of high-entropy carbides can be used to understand and predict their structure, properties, and stability. Using first principles calculations, the individual and temperature-dependent contributions of vibrational, electronic, and configurational entropies are analyzed, and compare them qualitatively to the enthalpies of mixing. As an experimental complement, high-entropy carbide thin films are synthesized with high power impulse magnetron sputtering to assess structure and properties. All compositions can be stabilized in the single-phase state despite finite positive, and in some cases substantial, enthalpies of mixing. Density functional theory calculations reveal that configurational entropy dominates the free energy landscape and compensates for the enthalpic penalty, whereas the vibrational and electronic entropies offer negligible contributions. The calculations predict that in many compositions, the single-phase state becomes stable at extremely high temperatures (>3000 K). Consequently, rapid quenching rates are needed to preserve solubility at room temperature and facilitate physical characterization. Physical vapor deposition provides this experimental validation opportunity. The computation/experimental data set generated in this work identifies “valence electron concentration” as an effective descriptor to predict structural and thermodynamic properties of multicomponent carbides and educate new formulation selections.

1. Introduction

In 2004, Cantor et al.^[1] and Yeh et al.^[2,3] changed the course of materials discovery in structural metallurgy by introducing the concept of entropic stability. An elegant approach to formulation design where the configurational entropy of 5 metals on a single sublattice becomes the thermodynamic anchor for phase stability. Since that report, thousands of papers were written, expanding this concept across broad regions of the periodic table.^[4] New alloys offering mechanical, electrical, irradiation, oxidation, and corrosion properties beyond those possible in conventional materials are emerging steadily.^[5–10] The underlying mechanism behind improved chemical, physical, and mechanical properties have been explained based on solid solution strengthening, high temperature stability, and selective high density, high strength scale formation, etc.^[5,9,10] While the specific role of entropy in these systems has been reconsidered, particularly in context of its enthalpic partner, solid solutions with multiple principal elements

remain an important research trajectory.

In 2015, inspired by the Cantor’s and Yeh’s original work, Rost et al. extended this configurational disorder concept to complex oxides, where an analogous set of five-cation oxide crystals were found.^[11] This work provided the first conclusive proof of entropic stabilization by formulation design, and thus a fundamentally sound foundation for entropy-engineered discovery. Following this work, the electronic, mechanical, magnetic, refractory, and energy materials communities explored new high-entropy systems in search of novel battery electrolytes, capacitor dielectrics, solar absorbers, ultrahigh temperature refractories, and magnets.^[12–19] In parallel, computational groups developed algorithms and approaches to predict what elemental combinations were amenable to configurational stabilization.^[17,20] Nonmetallic high-entropy systems clearly offer unexpected cation solubility in a large family of oxides, carbides, and nitrides. In addition, while finding a steady stream of new ones presents little difficulty, deciding which ones to find remains a more substantial challenge. Structure–property relationships in high-entropy systems are at an early development stage and knowledge generation in this area is needed.


M. D. Hossain, T. Borman, J.-P. Maria
Department of Materials Science and Engineering
The Pennsylvania State University
University Park, PA 16802, USA
E-mail: mzh606@psu.edu

C. Oses, M. Esters, C. Toher, S. Curtarolo
Center for Autonomous Materials Design and
Department of Mechanical Engineering and Materials Science
Duke University
Durham, NC 27708, USA

L. Feng, W. G. Fahrenholtz
Department of Materials Science and Engineering
Missouri University of Science and Technology
Rolla, MO 65409, USA

A. Kumar, J. M. LeBeau
Department of Materials Science and Engineering
Massachusetts Institute of Technology
Cambridge, MA 02139, USA

D. Brenner
Department of Materials Science and Engineering
North Carolina State University
Raleigh, NC 27695, USA

 The ORCID identification number(s) for the author(s) of this article can be found under <https://doi.org/10.1002/adma.202102904>.

DOI: 10.1002/adma.202102904

In this manuscript, we address this entropic-design challenge in the context of transition-metal carbides, a family of materials that generated substantial recent interest and research activity.^[17,21] Our approach uses “valence electron concentration” (VEC) as a generic discovery descriptor that indicates the average number of valence electrons per formula unit. We identify VEC for four reasons: i) simplicity—it requires only the periodic properties of the elements; ii) predictive connections between VEC to the mechanical properties of mono and binary carbides are well established,^[22,23] iii) VEC directly relates to the electronic structure, underpinning all physical properties;^[23–26] and iv) within a particular structure, VEC is a stability indicator.^[27]

Transition metal carbides are an ideal host for this approach. In many cases, their structures can be thought of as metal packing structures with C occupying interstitial sites, where metal–metal distances expand only modest amounts after full carbon incorporation. Consequently, most monocarbides can exist with a broad C:M (M = metal) ratio window, particularly on the carbon-deficient side.^[28] When engineering the metal formulation to include 5 species, the boost in configurational entropy further enhances stability of the single-phase state (all metal atoms on one sublattice). This enhanced solubility has been reported by numerous authors who observed that large fractions of W and Mo can be stabilized in the rock salt structure, even though monocarbides prefer a different stoichiometry and coordination.^[17,29] This expanded solution window underpins the present study because it expands the VEC range that one can achieve in a rock salt carbide, and it increases the possible set of unique formulations (and thus local structures) that can host the same VEC value.

To frame and better understand the utility of VEC, consider the pioneering work of van de Walle and co-workers who used it to explain why the highest melting point in the HfC-TaC composition family occurs close to the 25/75 composition ratio.^[26] HfC has a VEC value of four and the highest melting point of monocarbides. TaC has a lower melting point than HfC, thus one may expect a lower melting point from on-average slightly weaker bonds. This, however, is not the case. Substituting Ta for Hf adds additional valence electrons to the system since Ta originates from group 5. These additional electrons populate the metal d_{xy} , d_{xz} , and d_{yz} orbitals which are empty in pure HfC. Recall that in refractory metal carbides, due to the small carbon radius and their description as an “interstitial structure,” metal near-neighbor separation distances are similar to the distances in their parent metal structures with substantial metal orbital overlap along $\langle 110 \rangle$ directions. More valence electrons introduced between nearest and second-nearest neighbors offer greater overall stability and a higher melting temperature. Multiple researchers predicted that a VEC of 8.4 afforded the optimal combination of M–C and M–M bonding for overall stability in a rock salt carbide.^[23]

Thus, for a given structure, engineering the metal cation formulation will tailor the VEC, and in turn the overall stability and properties as influenced by a controlled population of electronic states about the Fermi energy. The expanded solubility in high-entropy carbides provides a new latitude to this process and guiding principle for entropic formulation design.

Table 1. List of nominal high-entropy carbide compositions sorted by valence electron concentration (VEC).

Designation	Composition	VEC/f.u.
HEC8.0	(HfScTaTiZr)C	8.0
HEC8.4	(HfNbTaTiZr)C	8.4
HEC8.6 _a	(HfNbTaTiV)C	8.6
HEC8.6 _b	(HfTaTiWZr)C	8.6
HEC8.8 _a	(HfMoTiWZr)C	8.8
HEC8.8 _b	(HfNbTaTiW)C	8.8
HEC9.0 _a	(NbTaTiVW)C	9.0
HEC9.0 _b	(HfMoTaWZr)C	9.0
HEC9.0 _c	(HfMoVWZr)C	9.0
HEC9.4	(MoNbTaVW)C	9.4

To validate this approach, however, the thermodynamic stability for high-entropy compositions must be evaluated to quantify the relative roles of enthalpy, and configurational, vibrational, and electronic entropy to the stabilization of a high symmetry high-entropy phase. While the VEC premise provides a convenient opportunity to design carbides and nitrides with enhanced chemical, physical, and mechanical properties, synthesis experience in these systems is modest at best. Many element formulations introduce challenges to making high quality materials and characterizing them robustly, as such, we present targeted advances to physical vapor deposition (PVD) film preparation as a companion to our density functional theory (DFT) calculations.

We designed the high-entropy carbide formulations listed in **Table 1** based on VEC with an objective to understand and scale the thermodynamic stability with VEC. The formulations offer a deliberate range of VECs and mixing enthalpies to facilitate comparison and understanding. First principles calculations were first used to calculate the enthalpies and entropies of all compositions to predict the transition temperature into the homogeneous solid solution state. The VEC descriptor quantifies the enthalpy and entropy evolution with electron population and describes thermodynamic stability. Calculations are supported by synthesis and phase evolution analysis. With these data and their analyses, we establish a universal VEC descriptor to predict high-entropy carbide free energy, structural parameters, and to indicate expectations for physical properties.

2. Results and Discussion

Based upon our team’s previous experimental and computational work, the formulations proposed in Table 1 were designed to enable the greatest spectrum of VEC values with stabilization in the rock salt structure. The latter is not guaranteed and depends on abilities to freeze in a high-temperature solid solution in systems for which phase separation is energetically favorable. Since five-or-more principal element mixtures can exsolve into multiple solid solutions, spinodal composites, or intermediate compound precipitates,^[30] the extent to which our current compositions tend toward solubility was

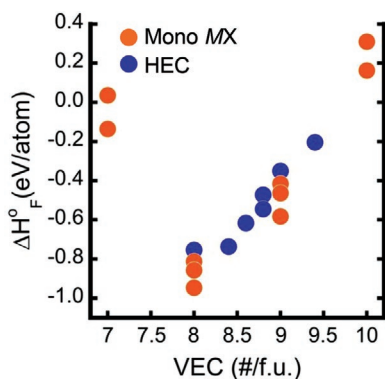


Figure 1. Formation enthalpy of high-entropy and mono carbides versus VEC.

first assessed using DFT calculations, the results of which are shown in **Figure 1**.

The calculations show that: i) the formation enthalpy of mono and quinary carbides increases gradually (i.e., becomes less favorable) as VEC increases above 8.0, and ii) for WC and MoC (VEC = 10) and YC (VEC = 7) formation enthalpies are positive. The latter indicating that carbides of W, Mo, and Y prefer a different structure, which is consistent with experimental findings and computational predictions.^[28] Overall, the data show that the enthalpic contribution to the stability of high-entropy carbides can be large, but is reduced by 0.55 eV atom⁻¹ when the VEC increases from 8.0 for (HfScTaTiZr)C≈HEC8.0 to 9.4 for (MoNbTaVW)C≈HEC9.4.

The electron density of states (e-DOS) of a prototypical group-IVB rock salt monocarbide is shown in **Figure 2** (top blue trace, referenced as MC). The feature of prime importance is the DOS minimum, which is referred to as the pseudogap (E_{pg}), and references the zero-energy state. The E_{pg} indicates the transition in energy space between bonding states ($E < E_{pg}$) and antibonding states ($E > E_{pg}$). When E_{pg} and the Fermi level (E_F) overlap, all bonding states are full, and all antibonding states are empty. The vertical lines (red) indicate the relative location of E_F with respect to E_{pg} for IIIB, IVB, VB, and VIB monocarbides, and how their relative filling ratio of bonding to antibonding states depends on group number: adding elements lower than IVB introduce empty bonding states, higher than IVB populate antibonding states (the exact e-DOS shape will change for individual materials, but overall structures are very similar). These filling fractions and energy trends will be used to rationalize thermodynamic stability and entropic contributions of high configurational entropy formulations.

Calculated e-DOS profiles for our high-entropy formulations are also presented in **Figure 2**, arranged from bottom to top in order of increasing VEC. For HEC8.0 (where VEC = 8) all bonding states are filled and all antibonding states are empty, consequently, formation enthalpy is minimized (the trend that is illustrated in **Figure 1**). When VEC exceeds eight, antibonding states become filled, the E_F shifts to the right, and the enthalpy of formation becomes less negative. The relationship between the number of filled antibonding states and the enthalpy of formation for this carbide formulation series is presented in **Figure 3**. The number of antibonding states were calculated from the area between the pseudogap energy and Fermi

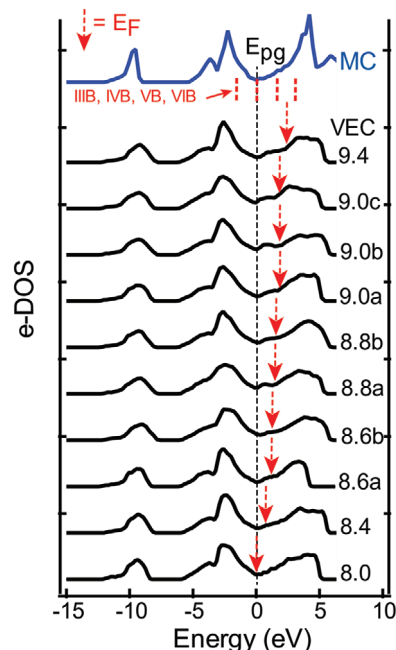


Figure 2. Prototypical electronic structure (e-DOS) of a mono transition metal carbide in the rock salt structure (top trace in blue-referenced MC). The vertical lines (red) represent the Fermi levels of prototype mono carbides. The e-DOS are also plotted as a function of increasing valence electron concentration for the 5-cation carbides in Table 1 (trace in black). The vertical black dotted line is the pseudogap (E_{pg}) and vertical red arrow indicates the Fermi level (E_F). The pseudogap is the zero-energy reference state and demonstrates a systematic shift in Fermi level position with VEC. As a consequence, materials bonding characteristics and thermodynamic properties evolve with VEC.

level and plotted against formation enthalpy. The relationship is roughly linear with increasing antibonding states eroding enthalpic stability. These calculations and analyses demonstrate how VEC becomes a generic and easily calculated descriptor of high-entropy carbide enthalpic stability, that is easily estimated by periodic trends of the cation collection and the net stoichiometry.

While this treatment provides an important baseline, it is only a zero-Kelvin reference. Predicting thermodynamic stability at finite temperature requires that one combine formation

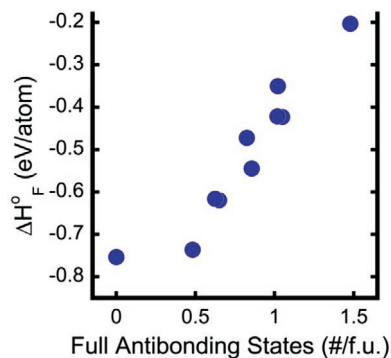


Figure 3. High-entropy carbide formation enthalpy versus filled antibonding state fraction.

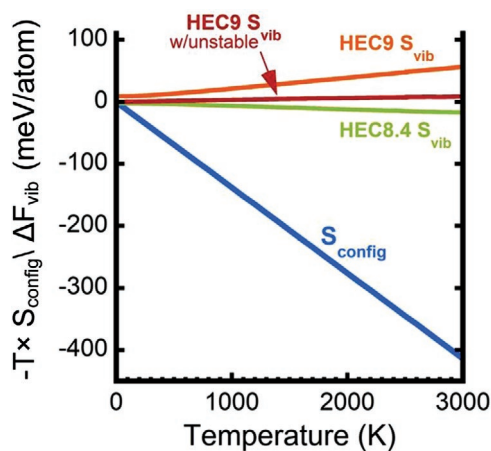


Figure 4. Temperature dependent configurational formation entropy and vibrational free energy of five-cation rock salt crystals HEC8.4 and HEC9_b.

enthalpies with configurational, vibrational, and electronic free energies. We begin this process by computing the configurational entropy of a rock salt crystal with five metals populating the cation sublattice at random as shown in **Figure 4**.

The next contribution to consider is the vibrational formation entropy. **Figure 4** also shows the temperature dependent free energy values calculated for HEC8.4 and HEC9_b. The vibrational entropy contribution associated with these disordered crystals is calculated with reference to the starting monocarbides having the rock salt crystal structure. To fully interpret the predictive power of the calculations, it is important to recall that MoC and WC are not stable in this structure. Consider first the predictions for HEC8.4, containing only cations that do form stable rock salt carbides; the vibrational formation entropy is small but negative and therefore it contributes to stability. This result is anticipated upon considering a broad, though complicated body of literature showing that vibrational entropy in chemically disordered crystals depends on structure, bond types, mass distributions, force constant fluctuations, relative crystal volume, and atomic size mismatches.^[31–39] While the behavior is complex and individual contributions may compete, the general expectations is that the amalgam of chemical disorder will produce an overall softer lattice and enhance vibrational entropy by generating new lower frequency modes.^[31–39]

The behavior in HEC9_b, however, is different; in this formulation, the vibrational formation energy contribution is positive offering a net destabilizing effect. We can rationalize this difference by considering the energetically unfavorable reference states of rock salt MoC and WC. Of the 49 configurations that were generated using AFLOW's POCC algorithm to calculate the vibrational spectrum, several were mechanically unstable because of the resistance from W and Mo to form face-shared octahedral networks at high concentrations. However, they are included because, while they are not stable as a bulk crystal, they can exist locally, where they are prevented from distorting by the surrounding stable configurations, and thus participate in the overall structure. This mechanical instability manifests in reduced vibrational degrees of freedom and a positive vibration formation entropy. As a demonstration exercise,

the calculation was made without the unstable configurations (also shown in **Figure 4**) and its value approached zero.

Assigning specific contributions or mechanisms to vibrational disorder as predominant is outside the scope of this paper, but irrespective of their origin, their influence on stabilization is very modest, even at high temperatures. While this result is somewhat expected, explicit testing and validation is to date unreported and an important contribution to the literature and a fundamental understanding of thermodynamic stability. We note that given the computational expense of phonon mode calculations, this study was limited to two formulations, HEC8.4 and HEC9_b, because they “bracket” the formation enthalpy spectrum and provide initial insights into thermodynamic trends.

The next step in our thermodynamic construction is to calculate the electronic entropy, which is determined by the VEC and the Fermi level position in the e-DOS. The Fermi–Dirac distribution sets the electronic occupation as a function of temperature and the e-DOS slope determines the rate at which electronic disorder increases. When VEC is large and $E_F > E_{pg}$, the total population of electrons is higher and the e-DOS slope is generally positive: increasing temperature shifts the energy distribution to a region of more available states. This predicts maximum electronic disorder with VEC (this result is shown in **Figure S1**, Supporting Information), but calculating the formation entropy and formation free energy requires a reference of the component monocarbides. For these calculations, we considered the possibilities where the five-component solid solutions formed from their monocarbides in: i) the rock salt phase (**Figure 5** (blue traces)), and ii) in their respective thermodynamically stable phases (**Figure 5** (orange traces)).

The data in **Figure 5** show that electronic entropy contributions stabilize some compositions (HEC8.4, 8.6_a, 8.6_b, 8.8_b, and 9.0_a), while destabilizing others (HEC8.0, 8.8_a, 9.0_b, 9.0_c, and 9.4) when the precursor monocarbides are in the rock salt structure. To understand this, consider that rock salt monocarbides with very low or high VEC values, such as ScC/YC and MoC/WC, have E_F in a steeply sloped region of the e-DOS (see **Figure 2**) where the electronic entropy is large. Reacting into a solid solution carbide drives E_F closer to E_{pg} , a flatter region of the DOS where electronic disorder is lower. As a consequence, high entropy compositions with multiple high and/or low VEC constituents experience an electronic entropy penalty. High entropy compositions where these “outlier” constituents are absent have a small and negative electronic entropy return. In the second method, we consider formation when MoC and WC are hexagonal $P\bar{6}m2$ and Sc₃C₄ as tetragonal $P4/mnc$. The temperature dependent results are also shown in **Figure 5**. Using this reaction all formulations exhibit either negative or near-zero electronic free energy. Moreover, higher VEC compositions have generally larger electronic contributions to stability; for example, ≈ 20 meV atom⁻¹ at 3000 K in HEC9.4. As with the vibrational contribution, the absolute value of electronic entropy is substantially smaller than the configurational component in all formulations. However, short-range ordering effects to the electronic entropy are negligible as shown in **Figure S2** (Supporting Information).

In summary, these thermodynamic calculations support that the periodic properties of the elements enable one to design

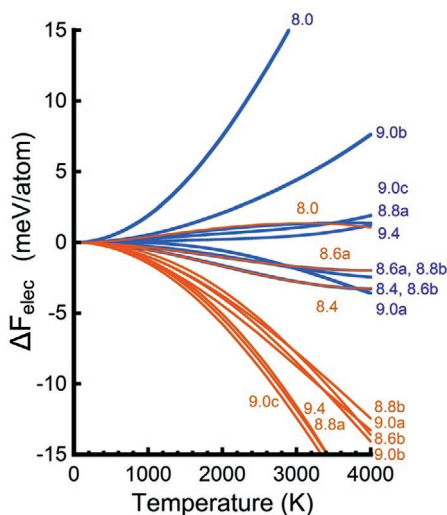


Figure 5. Temperature dependent electronic free energy of HEC formulations with reference to rock salt mono carbide precursors (blue traces) and to equilibrium mono carbide precursors (orange traces).

carbide formulations with a VEC that transitions, in the ideal thought experiment, continuously between 7 and 10. Adding reference knowledge regarding the component monocarbides informs the formation reactions that in turn guide formation enthalpy and entropy predictions, where the latter include configurational, vibrational, and electronic contributions, and ultimately a comprehensive calculation of thermodynamic stability. **Figure 6** shows summary result where Gibbs formation free energies are shown for the constituent monocarbides and our 10 candidate formulations presented as a function of VEC—the four plots represent equilibration at 1000, 2000, 3000, and 4000 K, respectively.

There are general trends of particular note that are evident upon inspecting Figure 6: i) at temperatures less than or equal to 1000 K for the available VEC values of 8 and 9, monocarbides are globally stable—this is consistent with their very large formation enthalpy values and consistently strong metallic/covalent bonding character; ii) as temperatures surpass 2000 K

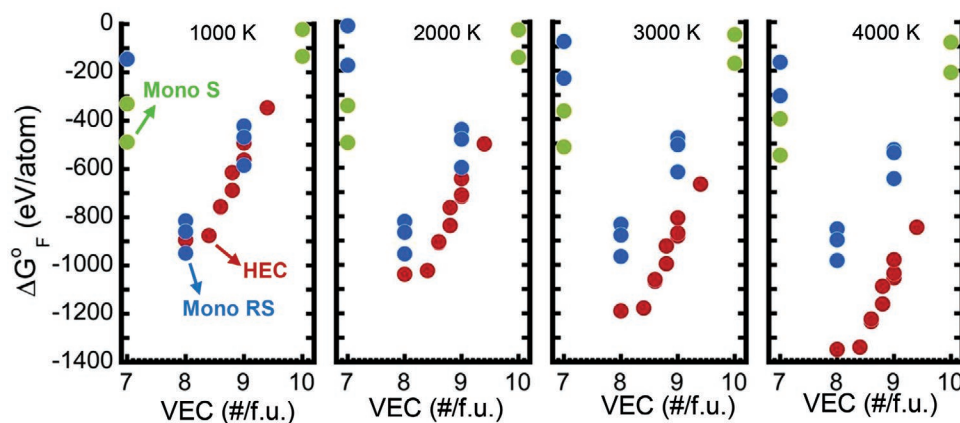


Figure 6. The Gibbs free energies at 1000, 2000, 3000, and 4000 K are plotted as a function of VEC. “HEC” refers to rock salt high entropy carbide and “Mono RS” represents rock salt III B, IV B, V B, and VIB mono carbides such as ScC, TiC, HfC, MoC, etc., and “Mono S” represents thermodynamically stable III B and VIB mono carbides, such as tetragonal Sc₃C₄ and hexagonal WC, etc.

(the region of scientific and technological interest for extreme refractory solids) the random solid solution structure becomes globally stable at all VEC because of its steep “entropic temperature slope”; iii) there is either a stability plateau or stability maximum between VEC = 8 and 8.5, this is consistent with multiple observations of melting point maxima in carbide solid solutions with VEC ≈ 8.4; and iv) increasing the temperature to the range spanning 3000 to 4000 K opens the free energy gap to a substantial margin suggesting a newly available material set to access this challenging temperature space. The Gibbs free energy data from 0 to 5000 K could be found in Figure S3 (Supporting Information).

The predictions above lead to a possible practical conundrum—we can predict materials with extreme high-temperature thermodynamic stability, but they are likely to be unstable at room temperature. Thus, while making them is possible, their low-temperature survivability and resilience against temperature cycling needs exploration. PVD affords us an ideal pathway to test this family of materials. Magnetron sputtering is a common member of the PVD family of approaches that is most often far from equilibrium by virtue of incoming adatom fluxes with 1–10 eV of kinetic energy and thus an effective temperature of 10⁵ K. Kotsonis et al. demonstrated how this effective temperature can produce the high-entropy solid solution crystals that are not accessible using bulk powder process methods.^[40] While the effective temperature of each adatom is large, the total heat deposited is small compared to the substrate, thus quenching occurs at rates approaching 10¹² K s⁻¹.^[41] For high-entropy carbide depositions, the substrate temperature is commonly set to 923 K, which is more than 2000 K below the melting point and 9000 K below the adatom effective temperature. While this temperature is low in the context of melting points, finite mass transport underneath the growth surface during deposition is a possibility that must be considered.

Following comparable approaches to carbide film deposition reported previously by our group, the structure and phase evolution of thin film high-entropy carbides were investigated experimentally as a direct companion to theory. While imperfect, the quenched growth conditions provide the best available approach to test the models. Eight of the ten simulated carbides

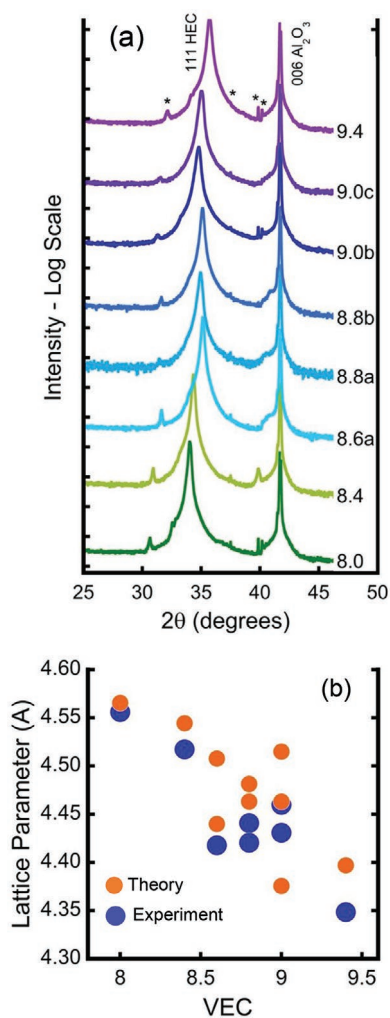


Figure 7. a) Offset XRD data of the high entropy carbide samples plotted with increasing valence electron concentration; b) experimental and calculated out-of-plane lattice constants.

were prepared, the compositions spanned the entire VEC spectrum from 8.0 to 9.4. As mentioned in the Experimental Section, carbide films were reactively sputtered from alloy metal targets in an Ar:CH₄ atmosphere using a HiPIMS plasma drive.

X-ray diffraction and the structural analysis data are presented in **Figure 7**, panel a) shows theta-two-theta patterns stacked in order of increasing VEC, all compositions exhibit single-phase rock salt structure with preferred <111>-crystallographic orientation. The sapphire (006) peak was used as an internal calibration standard to eliminate X-ray absorption and sample height adjustment errors. Panel b) shows the out of plane lattice constants from both experiment and DFT calculations, where experimental lattice parameters were calculated from the {111} reflection using Bragg's law.

Both the experimental and theoretical values show scatter at specific VECs, which we attribute to covalent radii diversity among the transition metals from the same group. Nevertheless, the lattice parameter trends in the disordered high-entropy carbide crystals, roughly linearly decreases with increasing VEC, follow the covalent radii trends of the transition metal

elements. This analysis establishes that the VEC is not only a good descriptor to predict the Gibbs' free energy of high-entropy materials, but it also captures crystal structure trends.

High entropy carbides homogeneity was further explored at nanometer scale by scanning transmission electron microscopy–energy-dispersive X-ray spectroscopy (STEM-EDS) analysis as shown in **Figure 8**. For the selected composition HEC8.4 ((HfNbTaTiZr)C), the elements are largely found to be uniformly distributed, with some Ti enrichment at the grain boundaries, as presented in **Figure 8a**. Furthermore, the atomic resolution high-angle annular dark-field and bright-field images in **Figure 8b** also substantiate sample uniformity in unit cell length scale. Notably, the high resolution image shows a large stacking fault population in the chemically disordered crystal which are also prevalent in mono/binary transition metal carbides.^[42,43] Understanding the defect chemistry specifically the underlying thermodynamics and kinetic factors that influences vacancy ordering in chemically disordered system is beyond the scope of the present study. The STEM analysis supports XRD findings on metastable single-phase solid solution formation.

Many examples exist where quenched growth from energetic plasmas can produce metastable phases, including carbides like rock salt WC, which is thermodynamically stable only above 2500 °C.^[44,45] Given these successes, we explored how and if VEC can be used to predict and understand synthesis trends under nonequilibrium conditions. Rock salt carbides are of particular interest for this study because they can accommodate up to ~40% carbon vacancies before gross structural instabilities. When deficiencies are sufficient, lower-symmetry metal-rich phases, such as Ta₂C (*P3̄m1*), Nb₂C (*P6₃/mmc*), and TiC_{0.59} (*R3̄mH*) become stable. Such transitions can be retarded to lower carbon stoichiometries by quenched growth from the vapor phase, thus it is interesting to explore if the low-carbon threshold below which separation occurs can be entropically tuned, and if said tuning can be rationalized by cation-VEC. We note that until now, we modified the cation formulation to modulate VEC. In the present experiment set we vary carbon concentration to demonstrate phase stability over a carbon deficiency window, and the impact of entropy, but we also change VEC by removing C. As such, the VEC in all cases will be lowered, but the VEC trend from the cation sublattice constituents will remain same. Generally speaking, in this context, when carbon deficiencies are large, high valence cations like W and Mo should provide more stability.

To test this hypothesis, we compared the structure evolution in TiC_x and HEC8.4≈(HfNbTaTiZr)C_x films where the carbon chemical potential is controlled by the methane partial pressure during reactive deposition. To do so, films were prepared from Ti and five-metal alloy targets at constant Ar flow of 20 sccm, but CH₄ flows spanning 0.2–3 sccm, all other conditions identical. X-ray data illustrating structural evolution trends are shown in **Figure 9**.

Consider first TiC from high to low methane flows: between 3 and 2 sccm, the carbide phase is rock salt with highest peak intensities between 2.0 and 2.2 sccm. Above this range, there is modest broadening that we associate with excess carbon. For a 1.8 sccm methane flow rate broad new peaks appear that can be indexed at TiC_{0.59}, a metal rich lower symmetry carbide phase (*R3̄mH*) in addition to the rock salt majority phase. As methane

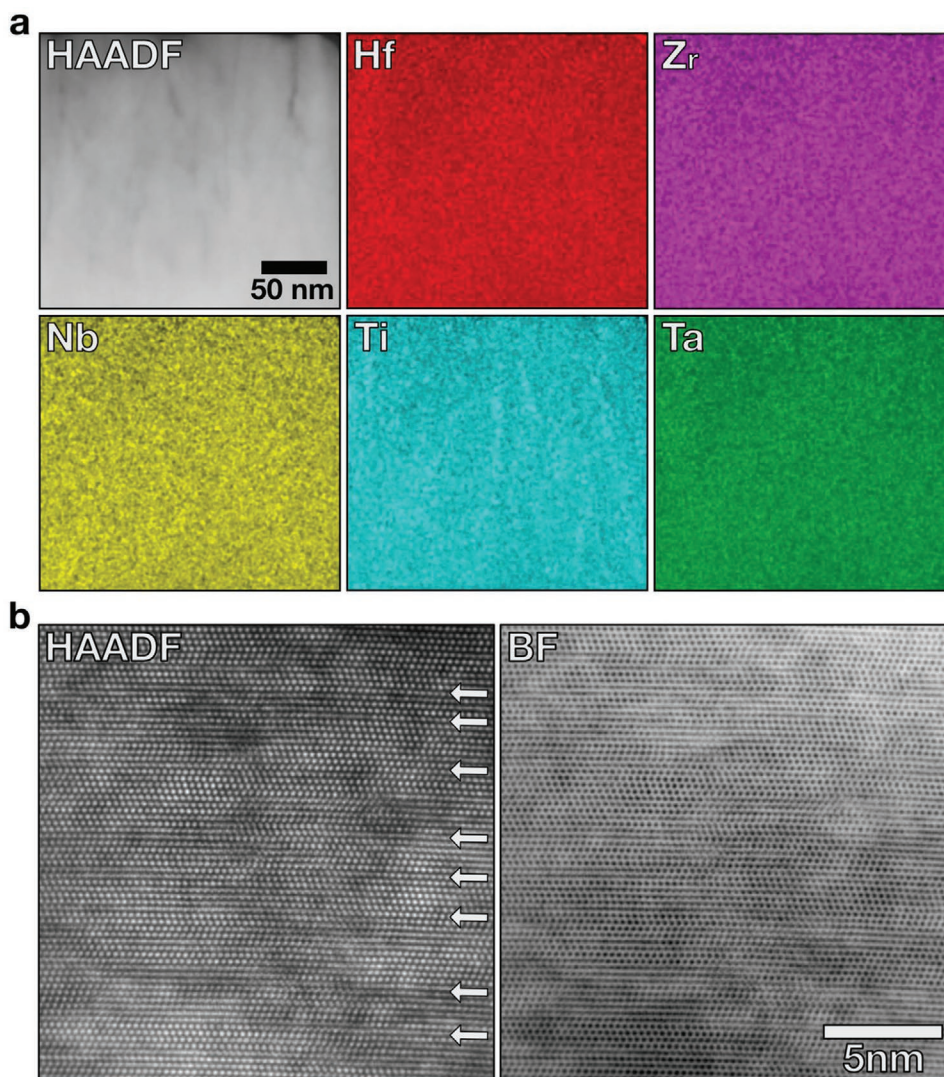


Figure 8. a) STEM-EDS elemental maps, b) high-angle annular dark field (HAADF) and bright-field (BF) STEM images of HEC8.4: (HfNbTaTiZr)C.

flow is further reduced to 0.2 sccm, three things occur: i) the rock salt phase peak intensities become monotonically lower, ii) the $\text{TiC}_{0.59}$ peak intensities remain relatively constant but disappear below ≈ 1.0 sccm, and iii) new peaks associated with carbon-containing Ti-metal emerge and intensify. Similar experiments were conducted with TaC (not shown) with the same phase evolution trends.

The same experimental deposition conditions were applied to $\text{HEC8.4} \approx (\text{HfNbTaTiZr})\text{C}_x$ depositions, the companion X-ray data are shown in Figure 9b and illustrate distinct behavior. A phase-pure (to the extent detectable by a laboratory X-ray diffractometer) rock salt carbide crystal is preserved to CH_4 flow rates as low as 1.5 sccm, followed by still-rock-salt diffraction patterns accompanied by increasing peak width, presumably due to stoichiometry deviations. A transition then occurs between 1.0 and 0.5 sccm to a carbon-containing BCC/HCP high-entropy alloy. Most notably, no evidence of metal-rich monocarbide phases is observed, despite their known stabilities under low carbon activity conditions as seen with TiC and

TaC in the present work. The phase instability versus CH_4 flow rate result can be interpreted in two ways: the high configurational entropy phase is stable with higher concentrations of vacant carbon sites compared to TiC, or the high configurational entropy cation plasma is more effective at scavenging C from the gas atmosphere. The average formation enthalpy of HEC8.4 is comparable to TiC as shown in Figure 2, thus we do not expect the second interpretation, but to support the former, X-ray photoelectron spectroscopy analysis of HEC8.4 and TiC at the beginning of phase separation was used to compute C:M ratios. For TiC prepared at 2.0 sccm (phase pure) and 1.8 sccm (detectable $\text{TiC}_{0.59}$) the stoichiometry was Ti_1C_1 and $\text{Ti}_1\text{C}_{0.9}$, respectively. For HEC8.4 prepared at 1.3 sccm (phase pure) and 1.0 sccm (peak shoulder indicating initial phase instability) the stoichiometry was $\text{M}_1\text{C}_{0.6}$ and $\text{M}_1\text{C}_{0.5}$, respectively. These direct measurements support that under these preparation conditions, the high-entropy formulation is 4 times more tolerant of C deficiency, and consequent change in VEC, in the rock salt phase.

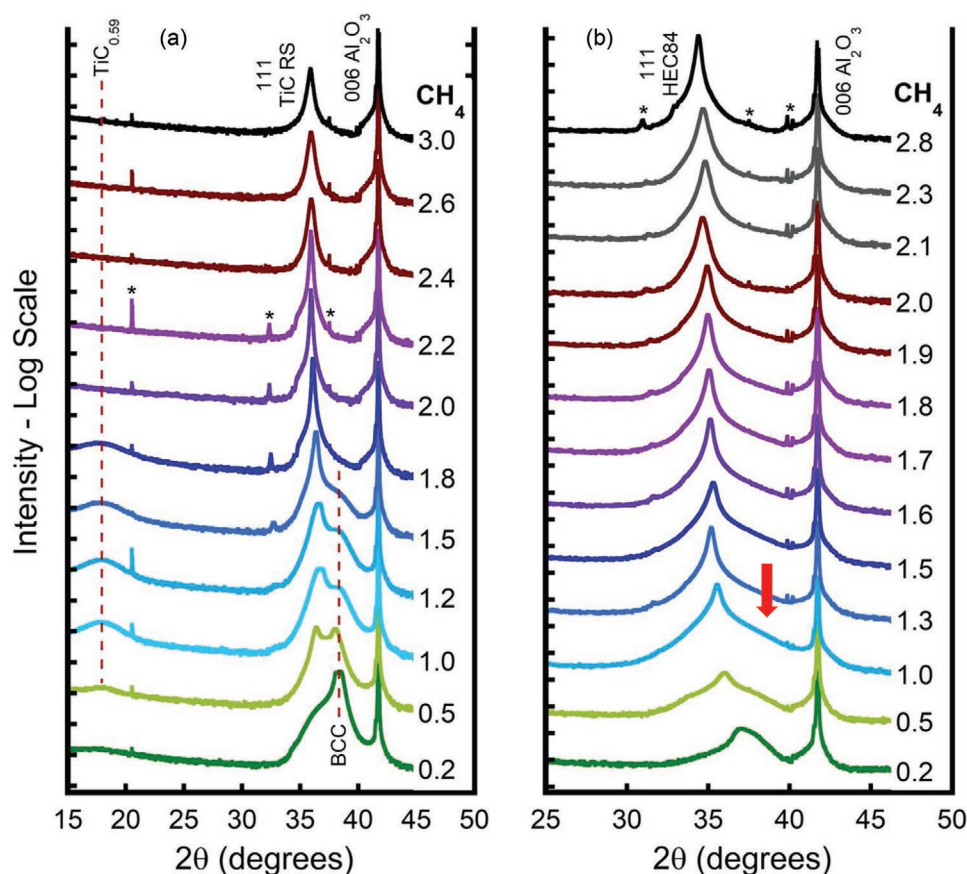


Figure 9. X-ray diffraction data are stacked with increasing methane flow rate for a) mono TiC_x and b) $\text{HEC8.4} \approx \text{Hf}_{0.2}\text{Nb}_{0.2}\text{Ta}_{0.2}\text{Ti}_{0.2}\text{Zr}_{0.2}\text{C}_x$. The red dashed lines in a) indicate $\text{TiC}_{0.59}$ and a BCC metal alloy while the red arrow in b) indicates a shoulder associated with an emergent BCC metal alloy phase.

In addition, chemically disordered crystals resist the formation of mixed intermediate phases. Formulations like $\text{HEC8.4}:(\text{HfNbTaTiZr})\text{C}_x$ can exsolve into thermodynamically stable rock salt ternary carbides such as $(\text{HfZr})\text{C}_x$, $(\text{ZrTi})\text{C}_x$, $(\text{TaNb})\text{C}_x$, and $(\text{TaTi})\text{C}_x$ but no X-ray data to date supports precipitation. To identify the equilibrium transition temperature above which the solid solution is favored over intermediates, temperature dependent Gibbs free energies were calculated and predict that above 2000 K, HEC8.4 is the most stable configuration—the results are shown in Figure S4 (Supporting Information). As discussed above, for PVD HECs, the kinetic energy of incoming species provides an effective temperature in the range of 10^5 K, and a TS term sufficient to stabilize the high configurational entropy structure. In this scenario, the comparatively modest substrate temperature of 650°C must not be sufficient to promote phase separation due to kinetic limits. To buttress our argument of a quenched high-entropy state, we subjected several compositions to postdeposition annealing and explore the onset of exsolution. **Figure 10** shows X-ray diffraction patterns for as-deposited HEC8.0 , HEC8.4 , HEC8.6_a , and HEC9.4 and the same compositions annealed for 1 h at 1400°C in a graphite furnace under flowing forming gas. At 1400°C , the lower VEC high-entropy carbides, HEC8.0 , and HEC8.4 , retain the rock salt high-entropy phase.

In contrast, phase separation is evident for HEC8.6_a and HEC9.4 . For HEC9.4 , hexagonal $\text{Mo}_2\text{C}/\text{W}_2\text{C}$ precipitates,

whereas HEC8.6_a disintegrates into a multiphase (V_2C , Nb_6C_5 etc.) microstructure as shown in Figure 10. The pseudoplateau in energy, i.e., VEC 8.0–8.5 produce globally stable multi-component carbides but beyond that VEC range the positive enthalpy slope drives phase segregation. A more in-depth analysis of metastability will be the subject of a future publication, but the initial indication is that a larger VEC is an indicator of

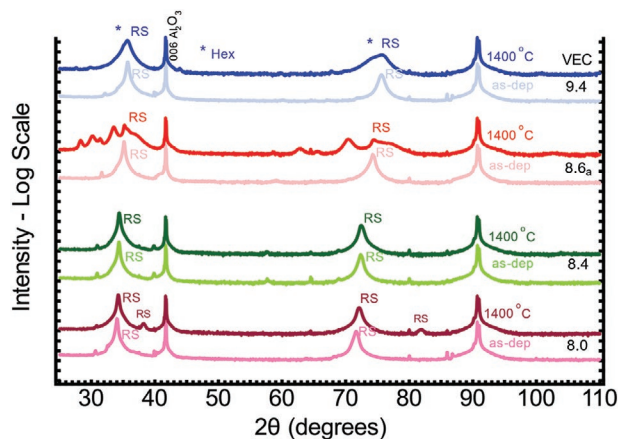


Figure 10. X-ray diffraction data of as deposited, and 1400°C annealed samples HEC8.0 , HEC8.4 , HEC8.6_a , and HEC9.4 ; these four compositions vary in VEC, classified to be 8.0, 8.4, 8.6, and 9.4, respectively.

lower enthalpic stability. These preliminary data points show in general terms that VEC can be used to predict exsolution trends from the high configurational disorder solid solution state. In this case, we do so by quenching a metastable solution and explore the subsequent temperature thresholds for phase separation. A metastable carbide with a higher VEC will have greater driving force for dissolution because of its lower formation enthalpy. In this manner VEC can also be used to understand synthesis trends, particularly in quenching conditions.

3. Conclusion

In this study, first principles calculations and physical vapor deposition method are combined to understand the fundamental stability criteria of high-entropy carbides. Density functional theory calculations predict that high-entropy carbides with a single-phase rock salt structure are thermodynamically stable at temperatures > 3000 K regardless of the combination of transition metals. In this temperature range, the configurational entropy contribution dominates the total free energy landscape and is two orders of magnitude larger than the electronic and vibrational entropies. This methodology enables the prediction of the ability to synthesize single phase high-entropy carbides considering only the enthalpy of formation and configurational entropy. Single phase high-entropy carbides compositions that are not stable in the rock salt structure such as (HfMoTaWZr)C and (MoNbTaVW)C are synthesized using PVD where large effective temperatures (10^5 K) of the plasma and low substrate temperature causes rapid quenching, on the order of 10^{12} K s⁻¹. This nonequilibrium process window produces single phase high-entropy carbides regardless of the stability of the constituents in that structure, which equilibrated to multiphase structures upon further annealing. At this point, PVD with its high effective temperatures and nonequilibrium synthesis conditions can be used to produce single-phase high-entropy carbides, but further study is needed to extend this synthesis to other compositions (e.g., borides) and identify processing parameters that will enable bulk synthesis of metastable phases. The VEC formulation is a simple but powerful methodology that predicts high-entropy carbides' thermodynamic properties, lattice parameter, disordered state transition temperature, synthesizability, metastability, etc. Accordingly, based on the VEC descriptor and electronic population, one can design new high-entropy carbides to procure desired chemical, physical, mechanical, and thermal properties.

4. Experimental Section

DFT calculations were performed with the Vienna Ab initio Simulation Package (VASP) v5.4.1.^[46,47] For high entropy carbides, 80-atom supercells were used to calculate the enthalpy and electronic entropy. Metal elements were randomly distributed across the cation sites using the special quasirandom structure generation module in the Alloy Theoretic Automated Toolkit (ATAT) package.^[48] Calculations were repeated three times with different 80 atom supercells to obtain appropriate statistics. This supercell selection ensures a stoichiometry (equiatomic composition) that maximizes the configurational entropy. A $2 \times 2 \times 2$ k-point grid based on the Monkhorst-Pack scheme was used to calculate

energies (convergence with respect to number of k-points was checked) and a $6 \times 6 \times 6$ k-point grid was used to generate electronic structures. The energy cutoff was set to 520 eV in both instances. Gaussian type smearing was used for DFT calculations and the smearing width was 0.1 eV. Monocarbide calculations were also performed for IIIV, IVB, VB, and VIB transition metal carbides in the rock salt (*Fm $\bar{3}m$*) (8 atoms per unit cell) phase—regardless of their thermodynamic stability in that structure. First principles calculations were also performed for the thermodynamically stable hexagonal (*P $\bar{6}m2$*) VIB, MoC, and WC, IIIB tetragonal (*P4/mnc*) Sc₃C₄, and orthorhombic (*Pbam*) Y₄C₅ carbide phases. The group IIIB, IVB, VB, and VIB transition metal carbides in the rock salt structure (monosystem) data provide an appropriate basis for comparison with the structure of high-symmetry multicomponent carbides phase. The calculated energies were compared with the AFLOW database.^[49,50] The enthalpy and entropy terms were calculated as follows:

Enthalpy of Formation, (H_f^0): Energies of all the mono and high-entropy compositions were calculated from a fully relaxed structure, using the graphitic phase for carbon. The standard enthalpy of formation, ΔH_f^0 , is given by

$$\Delta H_f^0 = E_{MC} - E_M - E_C \quad (1)$$

where E_{MC} is the energy of a high-entropy or monocarbide compound, E_M is the chemical potential of the metal, and E_C is the chemical potential of carbon. The formation enthalpies only consider internal energy contributions and are calculated from the differences in DFT-energies between the disordered approximate and the bulk elements. The temperature dependence of the enthalpies of formation was not considered under the first principles calculation scheme.

Configurational Entropy, S_{config} : The configurational entropy was estimated from the ideal entropy of mixing equation

$$S_{config} = -k_B \sum_{i=1}^N c_i \log(c_i) \quad (2)$$

where k_B is the Boltzmann constant, N is the number of species (5), and c_i is the mole fraction of constituent i (0.2). All presented data approximated a true random distribution of the cations. In real systems, short- and long-range ordering, preferential cation clustering, and grain boundary segregation have been reported in high-entropy structures, but those phenomena were not included in the first principles calculations described herein.

Electronic Entropy, S_{elec} : The electronic entropy was calculated from the electronic DOS, using the Fermi–Dirac distribution function to describe the occupation as a function of temperature (T).^[51]

The temperature-dependent electronic entropy, $S_T(E)$, is given by^[51]

$$S_T(E) = -k_B \int \left(D(E) \left(f_T(E) \log f_T(E) + (1 - f_T(E)) \log(1 - f_T(E)) \right) \right) dE \quad (3)$$

where $D(E)$ is the electronic DOS and $f_T(E)$ is the Fermi–Dirac distribution function

$$f_T(E) = \frac{1}{1 + e^{\frac{E - E_F}{k_B T}}} \quad (4)$$

where E_F is the Fermi energy and k_B is the Boltzmann constant.

Electronic Free Energy, F_{elec} : The electronic free energy was calculated as^[51]

$$F_{elec} = U_{elec} - TS_{elec} \quad (5)$$

$$U_{elec} = \int dE D(E) (f_T(E) - f_0(E)(E - E_F)) \quad (6)$$

$$S_{elec} = -k_B \int dE D(E) S_T(E) \quad (7)$$

The electronic Gibbs free energy was calculated from the difference between the electronic free energy of the high-entropy carbides and the average electronic free energy of the constituent monocarbides.

Vibrational Energy, F_{vib} : The vibrational contribution to the Gibbs free energy, F_{vib} , is given by

$$F_{\text{vib}}(T) = \int_0^{\infty} \left[\frac{\hbar\omega}{2} + k_{\text{B}}T \log \left(1 - e^{-\frac{\hbar\omega}{k_{\text{B}}T}} \right) \right] g(\omega) d\omega \quad (8)$$

where ω is the phonon frequencies and $g(\omega)$ is the phonon density of states. In this work, F_{vib} was calculated using the Debye–Grüneisen model as implemented in the Automatic Gibbs Library (AGL) module of AFLOW.^[52–54] For the high-entropy carbides, the AGL calculations were performed for an ensemble of configurations generated using AFLOW's Partial OCCupation (POCC) algorithm^[53] and thermally averaged as described in refs. [1] and [29], using an effective “synthesis” temperature of 10^5 K. AGL fits the DFT-calculated energies for a set of isotropically expanded and compressed volumes, $E_{\text{DFT}}(V)$, either numerically or to an equation of state to obtain the bulk modulus as a function of volume $B(V)$, which is then used to calculate the Debye temperature as a function of volume

$$\Theta_{\text{D}}(V) = \frac{\hbar}{k_{\text{B}}} \left[6\pi^2 V^{\frac{1}{3}} n \right]^{\frac{1}{3}} f(\nu) \sqrt{\frac{B(V)}{M}} \quad (9)$$

where n is the number of atoms in the cell, M is the cell mass, and $f(\nu)$ is a function of the Poisson ratio ν calculated using the bulk and shear moduli obtained from the elastic tensor generated by the Automatic Elasticity Library.^[52] The Debye temperature was then used to calculate the vibrational free energy using the following approximation

$$F_{\text{vib}}(V, T) = nk_{\text{B}}T \left[\frac{9}{8} \frac{\Theta_{\text{D}}(V)}{T} + 3 \log \left(1 - e^{-\frac{\Theta_{\text{D}}(V)}{T}} \right) - 3 \left(\frac{T}{\Theta_{\text{D}}(V)} \right)^3 \int_0^{\frac{\Theta_{\text{D}}(V)}{T}} \frac{x^3}{e^x - 1} dx \right] \quad (10)$$

$F_{\text{vib}}(V, T)$ was added to the $E_{\text{DFT}}(V)$ and pV terms to obtain the Gibbs free energy as a function of volume. The volume minimizing the Gibbs free energy is the equilibrium volume for that temperature and pressure, and that value is used to calculate $F_{\text{vib}}(T)$.

Gibbs Free Energy, (ΔG°): The Gibbs free energy was calculated from the enthalpy formation and the three entropic contributions to the free energy-

$$\Delta G^{\circ} = \Delta H_{\text{f}}^{\circ} + \Delta F_{\text{vib}} + \Delta F_{\text{elec}} - T\Delta S_{\text{config}} \quad (11)$$

Synthesis: Thin films were synthesized using high power impulse magnetron sputtering (HiPIMS). The HiPIMS plasma operated with a discharge voltage of -700 V, a pulse width of $40 \mu\text{s}$, and a duty cycle that was varied to maintain an average power of 250 W on the 50 mm diameter target. A $190 \mu\text{s}$, $+20$ V pulse was applied $4 \mu\text{s}$ after the end of the main pulse to provide additional adatom energy and reduce target poisoning. Equiatomic metal alloy targets (99.5%, ACI Alloys) served as the metal source for the carbide compositions listed in Table 1. The targets were sputtered in 99.999% Ar (7.5 mTorr) with a variable CH_4 flow rate as the carbon source. The CH_4 flow rate was varied to achieve a stoichiometric metal-to-carbon ratio for each composition.^[55] All films were deposited on *c*-sapphire substrates at 650 °C, film thickness was 300 nm. Annealing was conducted in a resistance-heated furnace (Model 3060, Thermal Technology, Santa Rosa, CA) where thin films were heated at 10 °C min^{-1} from room temperature to 1400 °C, held for 1 h then cooled at 10 °C min^{-1} .

X-Ray Diffraction: X-ray diffraction patterns were collected with a Panalytical Empyrean X-ray diffractometer operating a copper X-ray source at 45 kV and 40 mA. Data were collected in Bragg–Brentano

geometry using a HDBB incident beam optic with 0.125° and 0.5° divergence and antiscatter slits in the incident side and a 0.25° divergence slit before the Pixel area detector operated in scanning line mode. X-ray scattering angles were 10° – 120° and X-ray energy was 8.04 keV. The phase analysis were conducted with HighScore Plus software.^[56]

STEM: Cross-sectional samples of high-entropy carbide thin films were prepared for electron microscopy by mechanical wedge polishing and final thinning using cryogenic Ar-ion milling. STEM imaging and EDS were performed with a probe corrected Thermo Fisher Scientific (TFS) Themis Z G3 60–300 kV operated at 200 kV with a probe convergence semiangle of 18 mrad. A collection semiangle range of 63 – 200 and 0 – 35 mrad were used for high-angle annular dark field (HAADF) and bright-field (BF) STEM imaging. The EDS data were collected with a TFS Super-X detector and analyzed using the TFS Velox software.

Supporting Information

Supporting Information is available from the Wiley Online Library or from the author.

Acknowledgements

This research was funded by the U.S. Office of Naval Research Multidisciplinary University Research Initiative (MURI) program under Grant No. N00014-15-1-2863. Computations for this research were partially performed on the Pennsylvania State University's Institute for Computational and Data Sciences' Roar supercomputer. J.M.L. and A.K. acknowledge funding from the Air Office of Scientific Research (No. FA9550-20-0066). A.K. further acknowledges support through a MIT MathWorks Engineering Fellowship. T.B. acknowledges the funding from National Science Foundation Graduate Research Fellowship- Grant No. DGE-1255832. Support for W.G.F. was provided by the National Science Foundation through grant CMMI-1902069 and L.F. was supported by the Enabling Materials for Extreme Environments signature area at Missouri S&T. This work was carried out in part through the use of the Characterization nanofacility at MIT. Any opinions, findings, and conclusions or recommendations expressed in this material are those of the authors and do not necessarily reflect the views of the Office of Naval Research and the National Science Foundation.

Conflict of Interest

The authors declare no conflict of interest.

Data Availability Statement

Research data are not shared.

Keywords

configurational entropy, electronic and vibrational entropy, free energy, high-entropy carbides, thermodynamic stability, valence electron concentration

Received: April 16, 2021

Revised: July 2, 2021

Published online: September 2, 2021

- [1] B. Cantor, I. T. H. Chang, P. Knight, A. J. B. Vincent, *Mater. Sci. Eng. A* **2004**, 375–377, 213.
- [2] J.-W. Yeh, S.-J. Lin, T.-S. Chin, J.-Y. Gan, S.-K. Chen, T.-T. Shun, C.-H. Tsau, S.-Y. Chou, *Metall. Mater. Trans. A* **2004**, 35, 2533.
- [3] J. W. Yeh, S. K. Chen, S. J. Lin, J. Y. Gan, T. S. Chin, T. T. Shun, C. H. Tsau, S. Y. Chang, *Adv. Eng. Mater.* **2004**, 6, 299.
- [4] D. B. Miracle, *JOM* **2017**, 69, 2130.
- [5] Y. Yin, Q. Tan, Y. Zhao, Q. Sun, Z. Shi, M. Bermingham, W. Zhuang, H. Huang, M. X. Zhang, *Corros. Sci.* **2021**, 180, 109190.
- [6] Q. Xu, H. Q. Guan, Z. H. Zhong, S. S. Huang, J. J. Zhao, *Sci. Rep.* **2021**, 11, 608.
- [7] Y. Zhang, T. T. Zuo, Z. Tang, M. C. Gao, K. A. Dahmen, P. K. Liaw, Z. P. Lu, *Prog. Mater. Sci.* **2014**, 61, 2002.
- [8] N. Hua, W. Wang, Q. Wang, Y. Ye, S. Lin, L. Zhang, Q. Guo, J. Brechtel, P. K. Liaw, *J. Alloys Compd.* **2021**, 861, 157997.
- [9] O. N. Senkov, G. B. Wilks, D. B. Miracle, C. P. Chuang, P. K. Liaw, *Intermetallics* **2010**, 18, 1758.
- [10] O. El-Atwani, N. Li, M. Li, A. Devaraj, J. K. S. Baldwin, M. M. Schneider, D. Sobieraj, J. S. Wróbel, D. Nguyen-Manh, S. A. Maloy, E. Martinez, *Sci. Adv.* **2019**, 5, eaav2002.
- [11] C. M. Rost, E. Sachet, T. Borman, A. Moballeggh, E. C. Dickey, D. Hou, J. L. Jones, S. Curtarolo, J.-P. Maria, *Nat. Commun.* **2015**, 6, 8485.
- [12] A. Sarkar, L. Velasco, D. Wang, Q. Wang, G. Talasila, L. de Biasi, C. Kübel, T. Brezesinski, S. S. Bhattacharya, H. Hahn, B. Breitung, *Nat. Commun.* **2018**, 9, 3400.
- [13] R. Witte, A. Sarkar, R. Kruk, B. Eggert, R. A. Brand, H. Wende, H. Hahn, *Phys. Rev. Mater.* **2019**, 3, 034406.
- [14] N. Oseniat, D. Bérardan, D. Dragoë, B. Léridon, S. Holé, A. K. Meena, S. Franger, N. Dragoë, *J. Am. Ceram. Soc.* **2019**, 102, 6156.
- [15] D. Bérardan, S. Franger, A. K. Meena, N. Dragoë, *J. Mater. Chem. A* **2016**, 4, 9536.
- [16] C. Oses, C. Toher, S. Curtarolo, *Nat. Rev. Mater.* **2020**, 5, 295.
- [17] P. Sarker, T. Harrington, C. Toher, C. Oses, M. Samiee, J.-P. Maria, D. W. Brenner, K. S. Vecchio, S. Curtarolo, *Nat. Commun.* **2018**, 9, 4980.
- [18] S. Zhai, J. Rojas, N. Ahlberg, K. Lim, M. F. Toney, H. Jin, C. Chueh, A. Majumdar, *Energy Environ. Sci.* **2018**, 11, 2172.
- [19] J. L. Braun, C. M. Rost, M. Lim, A. Giri, D. H. Olson, G. N. Kotsonis, G. Stan, D. W. Brenner, J. Maria, P. E. Hopkins, *Adv. Mater.* **2018**, 30, 1805004.
- [20] K. Kaufmann, D. Maryanovsky, W. M. Mellor, C. Zhu, A. S. Rosengarten, T. J. Harrington, C. Oses, C. Toher, S. Curtarolo, K. S. Vecchio, *npj Comput. Mater.* **2020**, 6, 42.
- [21] E. Castle, T. Csanádi, S. Grasso, J. Dusza, M. Reece, *Sci. Rep.* **2018**, 8, 8609.
- [22] K. Balasubramanian, S. V. Khare, D. Gall, *Acta Mater.* **2018**, 152, 175.
- [23] S. H. Jhi, J. Ihm, S. G. Loule, M. L. Cohen, *Nature* **1999**, 399, 132.
- [24] D. G. Sangiovanni, L. Hultman, V. Chirita, *Acta Mater.* **2011**, 59, 2121.
- [25] Y. Liang, Z. Gao, P. Qin, L. Gao, C. Tang, *Nanoscale* **2017**, 9, 9112.
- [26] Q. J. Hong, A. Van De Walle, *Phys. Rev. B: Condens. Matter Mater. Phys.* **2015**, 92, 020104.
- [27] J. Haglund, G. Grimvall, T. Jarlborg, A. F. Guillermet, *Phys. Rev. B* **1991**, 43, 14400.
- [28] T. B. Massalski, H. Okamoto, P. R. Subramanian, L. Kacprzak, *Binary Alloy Phase Diagrams*, ASM International, Materials Park, OH **1990**.
- [29] T. J. Harrington, J. Gild, P. Sarker, C. Toher, C. M. Rost, O. F. Dippo, C. McElfresh, K. Kaufmann, E. Marin, L. Borowski, P. E. Hopkins, J. Luo, S. Curtarolo, D. W. Brenner, K. S. Vecchio, *Acta Mater.* **2019**, 166, 271.
- [30] E. P. George, D. Raabe, R. O. Ritchie, *Nat. Rev. Mater.* **2019**, 4, 515.
- [31] L. Anthony, J. K. Okamoto, B. Fultz, *Phys. Rev. Lett.* **1993**, 70, 1128.
- [32] L. Anthony, L. J. Nagel, J. K. Okamoto, B. Fultz, *Phys. Rev. Lett.* **1994**, 73, 3034.
- [33] L. J. Nagel, L. Anthony, J. K. Okamoto, B. Fultz, **1997**, 18, 551.
- [34] N. Fultz, T. A. Stephens, W. Sturhahn, T. S. Toellner, E. E. Alp, *Phys. Rev. Lett.* **1998**, 80, 3304.
- [35] B. Fultz, L. Anthony, J. L. Robertson, R. M. Nicklow, S. Spooner, M. Mostoller, *Phys. Rev. B* **1995**, 52, 3280.
- [36] A. Van de Walle, G. Ceder, *Rev. Mod. Phys.* **2002**, 74, 11.
- [37] A. Van De Walle, G. Ceder, U. V. Waghmare, *Phys. Rev. Lett.* **1998**, 80, 4911.
- [38] A. van de Walle, G. Ceder, *Phys. Rev. B: Condens. Matter Mater. Phys.* **2000**, 61, 5972.
- [39] F. Körmann, Y. Ikeda, B. Grabowski, M. H. F. Sluiter, *npj Comput. Mater.* **2017**, 3, 36.
- [40] G. N. Kotsonis, C. M. Rost, D. T. Harris, J. P. Maria, *MRS Commun.* **2018**, 8, 1371.
- [41] D. Turnbull, *Metall. Trans. B* **1981**, 12, 217.
- [42] C. R. Weinberger, G. B. Thompson, *J. Am. Ceram. Soc.* **2018**, 101, 4401.
- [43] X. X. Yu, C. R. Weinberger, G. B. Thompson, *Acta Mater.* **2014**, 80, 341.
- [44] A. Pak, A. Sivkov, I. Shanenkov, I. Rahmatullin, K. Shatrova, *Int. J. Refract. Met. Hard Mater.* **2015**, 48, 51.
- [45] A. S. Kurlov, A. I. Gusev, *Inorg. Mater.* **2006**, 42, 121.
- [46] G. Kresse, J. Hafner, *Phys. Rev. B* **1993**, 47, 558.
- [47] G. Kresse, J. Hafner, *Phys. Rev. B* **1994**, 49, 14251.
- [48] A. Van De Walle, M. Asta, G. Ceder, *Calphad* **2002**, 26, 539.
- [49] C. Oses, C. Toher, S. Curtarolo, *MRS Bull.* **2018**, 43, 670.
- [50] C. Toher, C. Oses, D. Hicks, E. Gossett, F. Rose, P. Nath, D. Usanmaz, D. C. Ford, E. Perim, C. E. Calderon, J. J. Plata, Y. Lederer, M. Jahnátek, W. Setyawan, S. Wang, J. Xue, K. Rasch, R. V. Chepulsii, R. H. Taylor, G. Gomez, H. Shi, A. R. Supka, R. A. R. Al Orabi, P. Gopal, F. T. Cerasoli, L. Liyanage, H. Wang, I. Siloi, L. A. Agapito, C. Nyshadham, G. L. W. Hart, J. Carrete, F. Legrain, N. Mingo, E. Zurek, O. Isayev, A. Tropsha, S. Sanvito, R. M. Hanson, I. Takeuchi, M. J. Mehl, A. N. Kolmogorov, K. Yang, P. D'Amico, A. Calzolari, M. Costa, R. De Gennaro, M. B. Nardelli, M. Fornari, O. Levy, S. Curtarolo, in *Handbook of Materials Modeling* (Eds: W. Andreoni, S. Yip), Springer, Cham **2018**, pp. 1–28.
- [51] R. Feng, P. K. Liaw, M. C. Gao, M. Widom, *npj Comput. Mater.* **2017**, 3, 50.
- [52] C. Toher, C. Oses, J. J. Plata, D. Hicks, F. Rose, O. Levy, M. De Jong, M. Asta, M. Fornari, M. Buongiorno Nardelli, S. Curtarolo, *Phys. Rev. Mater.* **2017**, 1, 015401.
- [53] K. Yang, C. Oses, S. Curtarolo, *Chem. Mater.* **2016**, 28, 6484.
- [54] C. Toher, J. J. Plata, O. Levy, M. De Jong, M. Asta, M. B. Nardelli, S. Curtarolo, *Phys. Rev. B: Condens. Matter Mater. Phys.* **2014**, 90, 174107.
- [55] M. D. Hossain, T. Borman, J.-P. Maria, **2021**, <https://doi.org/10.13140/RG.2.2.19279.71848/1>.
- [56] T. Degen, M. Sadki, E. Bron, U. König, G. Nénert, *Powder Diffr.* **2014**, 29, S13.